ELSEVIER

International Journal of Heat and Fluid Flow 19 (1998) 1–9

International Journal of HEAT AND FLUID FLOW

Averaged and time-resolved heat transfer of steady and pulsating entry flow in intake manifold of a spark-ignition engine

Wolf-D. Bauer *, Joseph Wenisch, John B. Heywood

Massachusetts Institute of Technology, Sloan Automotive Laboratory, Rm. 31-064, Massachusetts Av. 77, Cambridge, MA 02139, USA

Received 3 April 1997; accepted 14 August 1997

Abstract

Entry flow heat transfer experiments are reported in steady and pulsating flows of air at mean Reynolds numbers of 3000–35,000. The ducts are chosen to match typical spark-ignition engine manifolds: a highly curved and a straight pipe, which together bracket most practical geometries. The pulsating engine intake flow encompasses an approximate half sine wave followed by a stagnant phase three times as long, all at a repetition rate of 16–50 Hz. Heat flow is imposed through electric heating of the outsides of the manifolds. Heat transfer in the curved pipe is closely comparable to the straight geometry, and it is concluded that entrance effects dominate. Time-averaged axially resolved and axially averaged Nusselt numbers are reported. The unsteady nature of the intake flow enhances heat transfer significantly, between 50% and 100%. Time-resolved wall heat flux measurements at a location close to the exit of the system show that heat transfer is delayed relative to the onset of the flow. During the stagnant flow phase, heat transfer and turbulence decay slowly from their high levels during the induction flow phase. Heat transfer enhancement in the pulsating flow case is caused by the contribution of the stagnant phase.

Keywords: Pulsating flow; Intake manifold; Internal combustion engine; Transient heat flux measurements

Notation

a	fitting parameter
A	area, amplitude ratio
A	after
AC	alternate current, generalized to time-varying component of heat flux signal
b	fitting parameter
B	before
BC	piston bottom center position
c	fitting parameter
c_p	specific heat at constant pressure
d	fitting parameter
D	hydraulic diameter
DC	direct current, generalized to mean component of heat flux signal
Dn	Dean number Re R/R_{pipe}
e	fitting parameter
h	heat transfer coefficient (W/m^2-K)
k	thermal conductivity (W/m-K)
L	length
$\dot{\bar{m}}$	time mean mass flow
MAP	intake manifold absolute pressure (temporal average) (bar)
Nu	Nusselt number hD/k
p	pressure
P	perimeter
Pr	Prandtl number ν/α
q	heat flux
R	half the hydraulic diameter; heat flow resistance
Re	Reynolds number UD/ν
rpm	engine crankshaft rotational speed (l/min)
S	engine stroke length
Sr	Strouhal number $\omega D/U$
t	time
T	temperature
TC	piston top center position
$\bar{u}_\tau$	time-mean friction velocity
U	velocity
x	axial position
y	distance from wall

Greek

α	variable
γ	ratio of specific heats
δ	Stokes layer thickness $(2\nu/\omega)^{1/2}$
Δ	increment
Λ	Stokes number R/δ
μ	dynamic viscosity (kg/m-s)
ν	kinematic viscosity (m^2/s)
ρ	density
φ	phase angle
ω	angular frequency

* Corresponding author. Tel.: +1 617 253 1792; fax: +1 617 253 9453; e-mail: wolf@mit.edu.

0142-727X/98/$19.00
PII: S0142-727X(97)10001-7

Subscripts

hyd	hydraulic
i	index
j	index
k	wave number
t	turbulent
x	axially resolved
δ	Stokes layer
$+$	inner variable, turbulence

Superscripts

$'$	per unit length
$''$	per unit area

Overscores

$\tilde{}$	time-varying component
$\bar{}$	axial or temporal average
$\dot{}$	per unit time

1. Introduction

This study concerns itself with the heat transfer of a pulsating entry flow into curved and straight pipes. Among other applications, such flows occur in the intake system of internal combustion engines and in the corresponding components of compressors. Heat transfer in the intake system is detrimental, because it lowers the breathing efficiency. For internal combustion engines, an additional interest arises: increased charge temperature causes higher chemical reaction rates leading to increased nitric oxide emissions and less tolerance to engine knock. Various features of the system investigated may influence heat transfer rates: entrance effects, pipe curvature, the unsteady flow, and pressure fluctuations. These have been investigated individually by many researchers.

Boelter et al. (1948) and Mills (1962) investigated entrance flows into straight pipes. Boelter controlled the wall temperature, while Mills imposed the wall heat flux. Otherwise, both experiments shared many features. Such entrance configurations as sharp edge, bellmouth, bend, and orifice plate were investigated. They found an approximate doubling of heat transfer close to the entrance, which then relaxed to the fully developed values for locations 10 or more pipe diameters downstream.

Curvature induces secondary flow patterns with the potential to increase heat transfer rates. Pratt (1947) and Schmidt (1967) correlated heat transfer as a function of the Dean number $\mathrm{Dn} = \mathrm{Re}R/R_{\mathrm{pipe}}$, where Re is the Reynolds number, R is half of the (hydraulic) diameter, and R_{pipe} is the pipe radius of curvature. Extrapolating their correlations for steady, fully developed flow to a lower value of R/R_{pipe}, as employed here, suggests that twice as much heat is transferred in a typical curved manifold pipe, as compared to a straight duct.

The temporal velocity distribution in the intake manifold runner of a four-stroke internal combustion engine is imposed by the intake valve timing and the piston velocity (a manifold runner is a single pipe connecting the manifold plenum to a cylinder). In an idealized cycle, the intake valve opens at a top center position of the piston for the duration of one down stroke, the induction stroke. While the intake valve is closed, the cycle continues for the duration of three strokes – compression, expansion, and exhaust. In total, the cycle corresponds to 720 crank angle positions or two revolutions of the crankshaft. During the induction stroke, piston velocity resembles a half sine wave with peak velocity approximately 1.6 times larger than the mean velocity, where $\bar{U}_{\mathrm{piston}} = 2 \times S \times \mathrm{rpm}/60$, and S is the stroke length. Continuity imposes the flow velocities in the intake manifold runner: $U_{\mathrm{duct}} = U_{\mathrm{piston}} A_{\mathrm{piston}}/A_{\mathrm{duct}}$. It follows that the peak and the mean flow velocity in the intake system are at a fixed ratio, and both scale with engine speed. Changes in mean mass flow rate (or mean Reynolds number) at a given engine speed are achieved by throttling the intake air. A typical volume of an intake manifold runner approximately equals the displacement volume of one engine cylinder. Hence, a manifold runner fills with fresh air over one induction process. The impact of acoustic phenomena is considered moderate and discussed separately.

Heat transfer in pulsating flow depends on variables describing the steady and unsteady components. For a constant Prandtl number, fluid dimensional analysis yields $\mathrm{Nu} = f(\bar{U}, \tilde{U}, R, \omega, \nu,$ waveform variables). $\bar{U}$ is the time- mean velocity, $\tilde{U}$ the amplitude of the oscillating velocity component, R the (hydraulic) pipe diameter, ω the oscillation frequency, ν the kinematic viscosity, and the waveform variables describe the velocity profile over one cycle. Most researchers choose the time-mean Reynolds number as one nondimensional group. Less agreement is found as to which is the most meaningful nondimensionalization of the frequency. Based on dimensional arguments, Arpaci et al. (1993) arrived at a correlation in $\overline{\mathrm{Sr}} = \omega D/\bar{U}$ and $A = \tilde{U}/\bar{U}$. They report heat transfer enhancement beyond a critical frequency $\omega_{\mathrm{critical}}$, which is independent of A (A ranged from small values up to about three). In analogy to the amplification or attenuation of turbulent bursting phenomena as a function of the flow pulsation frequency, Liao and Wang (1988) hypothesized a heat transfer rate dependency on $\overline{\mathrm{Sr}}_{\bar{u}_t} = \omega D/\bar{u}_t$. Because this group includes the mean friction velocity, it seems most applicable to flows where turbulence production sustains throughout the cycle. This is most likely to be true in flows with significant mean velocities ($\bar{U} \gg \tilde{U}$) and time mean Reynolds numbers larger than the critical value for steady turbulent flow. Liao and Wang categorized literature data according to their $\overline{\mathrm{Sr}}_{\bar{u}_t}$ values and found that heat transfer actually decreases for the intermediate range of the frequency parameter (in which their data lay). For large $\overline{\mathrm{Sr}}_{\bar{u}_t} > 1.58\,\mathrm{Re}^{0.125}$, Liao and Wang hypothesized that heat transfer increases over the corresponding quasisteady values. Condie and McEligot (1995) assumed that heat transfer is affected in a similar way by frequency as is the wall shear stress modulation. They postulate the importance of the group $\omega_+ = \omega\nu/\bar{u}_\tau^2$. Their experiments fell in the high frequency range of $\omega_+ > 0.08$, and they found very strong heat transfer enhancement over steady flow cases.

Most of the above researchers employed sinusoidal velocity fluctuations. However, the nondimensional frequency variables should still give indication whether heat transfer enhancement can be expected for the present flow configuration. Present values are estimated to be less than 0.01 of the critical value of ω_+ given by Condie and McEligot (1995) and approximately twice the suggested critical value of $\overline{\mathrm{Sr}}_{\bar{u}_t}$ by Liao and Wang (1988). Insertion of the expected parameter range into the correlation of Arpaci et al. (1993) indicates a heat transfer enhancement by a factor of two. Thus, it is uncertain if and to what extent heat transfer enhancement is to be expected. The current flow goes through a zero flow phase and resembles a reciprocating flow in that respect. The fluid mechanics of such flows have been investigated by a number of researchers. The occurrence of turbulence and relaminarization are expected to play an important role. Two groups were found to be important for characterization: the Stokes number $A = R/\delta$ and Re_δ, where $\delta = (2\nu/\omega)^{1/2}$ is the Stokes layer thickness, and Re_δ is based on the amplitude of the velocity fluctuation. However, to the knowledge of the authors, no correlations are available relating these parameters to heat transfer rates. The following paragraph reviews time-resolved fluid mechanics

and heat transfer results. In a separate section below, these are compared to time-resolved heat flux and velocity measurements from the system under investigation.

In reciprocating flows with large A, turbulence will appear during part of the cycle. Researchers consistently found a transition criterion of $Re_\delta \gtrsim 500$; e.g., Akhavan et al. (1991), who report that transition occurs late during the acceleration phase, with turbulence production persisting throughout the subsequent deceleration phase. Wall shear stresses in the turbulent part of the main flow phase are close to quasisteady values. Departure of the radial velocity profile from the laminar solution is especially apparent at the time of flow reversal. A laminar solution would exhibit regions of both positive and negative flow in the axial direction. These are no longer observed in the turbulent case because of stronger radial momentum exchange. Early flow acceleration prior to the onset of turbulence production then resembles a laminar start-up solution rather than a fully developed laminar oscillatory flow. The present case differs in that flow deceleration is followed by a stagnant phase, where one expects the transient growth of a shear free turbulent boundary layer. Malan and Johnston (1993) investigated heat transfer during the growth phase of such a boundary layer by direct numerical simulation. Their results showed that heat transfer enhancement is negligible during the initial growth phase and approximately approaches an asymptotic value for longer times. This increase in heat transfer rate ranged from 0.2 to 0.55 for initial turbulent Reynolds numbers (Re_t) of 60–380, respectively. For the present study, Re_t values of that order are expected. Accordingly, heat transfer during the stagnant portion of the flow should be elevated over purely diffusive heat transfer.

Practical intake flows also exhibit acoustic phenomena. However, their effect on convection velocities are limited, because the acoustic time scale (the frequency of a wave in a pipe of length 40 cm with an open and closed end is approximately 200 Hz) is faster than the time scale of the main flow (25 Hz). Hence, little impact on convective heat transfer can be expected. However, the pressure waves also cause temperature fluctuations even within the thermal boundary layers, which in turn induce heat fluxes. The magnitude and phasing of the heat flux fluctuations may be estimated by the analytical solution of Pfriem (1943).

$$\dot{q}_t'' = (k\rho c_p \omega_k)^{1/2} \frac{\gamma - 1}{\gamma} \overline{T} p_k \sin\left(\omega_k t + \varphi_k + \frac{\pi}{4}\right) \tag{1}$$

which is applicable for small sinusoidal pressure fluctuations with amplitude p_k, angular frequency ω_k, and phase angle φ_k. k, ρ, c_p, and γ are the thermal conductivity (and the wave number), density, specific heat at constant pressure, and the ratio of specific heats, respectively, of the gas, and $\overline{T}$ is the mean gas temperature. Because the governing equations are linear, this formula applies for each individual harmonic of a periodic pressure signal. Although these heat fluxes may be quite significant at any given time within the cycle, integration suggests that their net contribution over one cycle is zero.

Flows that simultaneously exhibit all these features have received relatively little attention. Borman and Nishiwaki (1987) reviewed the treatment of heat transfer in the intake system of internal combustion engines. They reported that standard pipe correlations were typically employed. Enhancement factors based on the intuition of the researchers were included to account for all of the above effects. The above review indicates the potential of individual flow features to enhance heat transfer; however, their possible interactions are not known. The review of pulsating flow gave a criterion for the occurrence of turbulence during parts of the cycle. However, it is not known when during the cycle this transition takes place. Because of this ambiguity, steady-state heat transfer correlations cannot be integrated to give the total heat transfer even if it behaved quasisteadily. Similarly, it can be expected that a diffusive solution with some turbulently enhanced mixing is appropriate during the stagnant portion of the cycle. However, the initial conditions are not obvious. Therefore, an experiment is conducted, which, for validation purposes, first aims at reproducing known results (steady entrance flow in a straight pipe) and then gradually adds complexity to the flow phenomena (curved pipe, and pulsating flow).

The experimental technique employed here resembles that of Condie and McEligot (1995). They determined heat transfer coefficients in the exhaust manifold of a motored engine modified to work as a reciprocating pump. Heat fluxes were imposed by an electric heater, and heat transfer coefficients were inferred from the wall-to-gas temperature difference. The current work also addresses the intracycle resolution of heat transfer by means of time-resolved measurements of heat flux and other relevant quantities.

2. Experimental apparatus

The experiments include both steady and pulsating flows employing a straight and a curved pipe. The steady flow experiment utilizes a pump to provide airflow. Mounting the manifold on a single-cylinder research engine sets up the pulsating flow. Table 1 summarizes geometric details and the valve timing events of the engine. Both pipes have a length of approximately 35 cm, corresponding to the dimensions of the manifolds of many production engines. The experimental setup employing the straight pipe is shown in Fig. 1, while the curved manifold is shown separately in Fig. 2. Table 2 lists their geometric parameters. Electrical resistance heaters 1.5-m long, wrapped at constant pitch along the axial length of the pipes, provide heat input. A 3-mm layer of glass cloth and a 2.5-cm cotton layer provide insulation around the outside. A 1-cm thick Teflon gasket insulates the downstream end of the pipe.

Using either pipe, their entries are connected to a tank in order to create a boundary condition that suppresses pressure wave dynamics upstream of that position. The tank has a hole of radius 1.25 cm larger than the outer radius of the upstream pipe flange. The flange is inserted into the opening so that it forms a flush surface with the tank side wall. A 3-mm thick silicone rubber sheet bridges the remaining gap. The sheet's inside diameter is clamped to the pipe flange, while the outer diameter attaches to the tank. This mounting serves as a thermal and mechanical insulator as well as a vacuum seal. Upstream of the tank, a throttle plate is installed to enable variation of the intake air density for engine experiments. A second, very large buffer tank is installed upstream of the throttle. Upstream of that tank, the mean flow rate is measured by a laminar flow meter.

Twenty K-type thermocouples measure the pipe wall temperature. They are glued with a thermally conductive adhesive

Table 1
Engine data

Stroke, cm	9.0
Bore, cm	8.3
Connecting rod length, cm	15.8
Compression ratio	10.14
IVO-0.1 mm lift	4° BTC
IVC-0.1 mm lift	56° ABC
EVO-0.1 mm lift	−48° BBC
EVC-0.1 mm lift	12° ATC

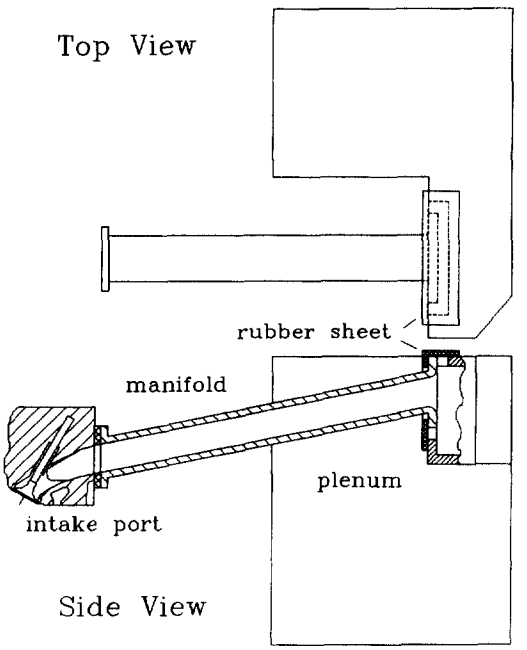

Fig. 1. Straight manifold mounted to test engine.

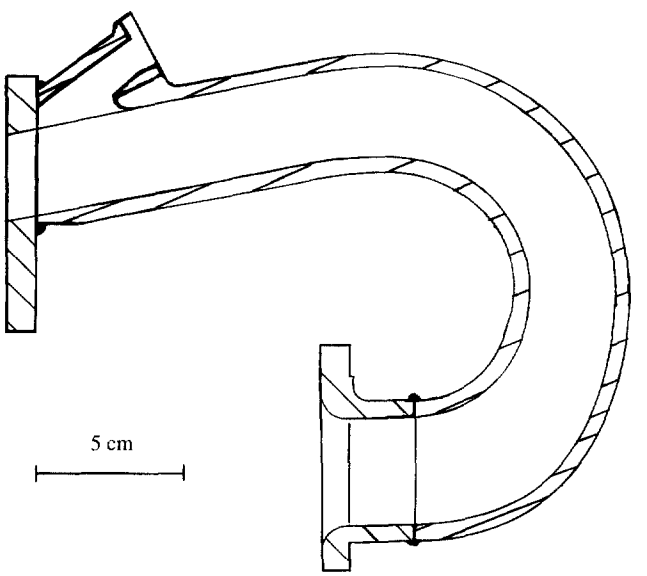

Fig. 2. Curved manifold pipe, cross section.

Table 2
Geometric parameters of manifolds

Manifold	Straight (cm)	Curved (cm)
Hyd. diameter	3.8	~4
Length	35	~35
Wall thickness	0.7	~0.3
Radius of curvature	–	5–25

to the outer surface of the manifold walls in five grouped locations along the manifold length. Each group consists of four thermocouples spaced evenly around the circumference, matching the pitch of the strap heater. Close to the exit, the straight pipe is fitted with an access hole for instrumentation, to accommodate – one at a time – a Vatell heat flux sensor, a Data Instruments pressure transducer, or TSI hot and cold wire probes. Adjacently, a thin film heat flux sensor from RdF Inc. is glued onto the inner surface of the duct. This square-shaped probe has a side length of 12 mm. The Vatell probe is a HFM 6 fast response thermopile (10 μs for 63% response to step input) deposited on an aluminium nitrite substrate of approximately 4-mm diameter and 25-mm length. The DC components of the heat flux measurements reported here are taken from the RdF probe, while the AC component is measured with the Vatell gauge. The signals of both heat flux probes lead into a Vatell amplifier. The voltage of the Vatell probe is further amplified by an Analog Devices unit to lift it well above the discretization floor of the data acquisition system. A PC-based data acquisition system logs all signals.

The cold and hot wires are TSI standard units, 1220 PI 2.5 and 1210-20, respectively. The former is used as a resistance thermometer, calibrated by a line fit to two points: ambient air and 100°C water vapor. The signal is first-order response corrected using a time constant of 2 ms. This value is derived from the energy balance and a standard heat transfer correlation for the wire filament. Below we see that this time constant matches the measured temperature signal sufficiently close for adiabatic temperature fluctuations, which is computed from measured pressure data. The hot wire is operated at constant temperature using a TSI 1750 unit. This system is calibrated for velocities higher than 3.5 m/s.

3. Calculation of heat transfer coefficients and error analysis

Heat transfer coefficients are calculated from their definition as the ratio of heat input per unit area to the gas-to-wall temperature difference. However, perfect insulation of the heated pipe along its outside surface cannot be achieved, because spatial constraints limit the amount of wrapping. Opportunities to insulate both ends are also restricted by choosing to mount the pipes to the cylinder head of the test engine in a realistic manner. Finally, significant heat redistribution caused by axial conduction is encountered as a result of using aluminium pipes of realistic wall thicknesses of 3 mm or more.

The loss and redistribution mechanisms are included into the energy balance equation used to evaluate the inside surface heat transfer coefficient h_{pipe},

$$\dot{q}'_{\text{heater}} + k_{\text{wall}} A_{\text{wall}} \frac{\mathrm{d}^2 T_{\text{wall}}}{\mathrm{d}x^2} = h_{\text{pipe}} P (T_{\text{wall}} - T_{\text{gas}}) + h_{\text{outside}} P (T_{\text{wall}} - T_{\text{ambient}}), \quad (2)$$

where P is the inside pipe perimeter. The wall temperature is fitted to a fourth-order polynomial, which allows computation of the second-order wall temperature derivative. By concurrently fitting appropriate wall temperature gradients at the upstream and downstream boundaries, conductive losses are incorporated into the analysis. In the presence of heat transfer to the interior, it is not possible to measure the wall temperature gradients accurately at the boundaries because of strong axial variation. However, they can be measured when eliminating this heat transfer mechanism. In both cases, the wall temperature gradients have to satisfy

$$k_{\text{wall}} A_{\text{wall}} \left. \frac{\mathrm{d}T_{\text{wall}}}{\mathrm{d}x} \right|_i = \frac{\Delta T_{\text{flange},i}}{R_{\text{flange},i}}. \quad (3)$$

where the $R_{\text{flange},i}$ and $\Delta T_{\text{flange},i}$ are the heat flow resistances and temperature differences across the insulations at the upstream and downstream ends of the pipe (silicone rubber sheet and Teflon gasket, respectively). Eliminating heat transfer to the in-

side by blocking the air passage, Eq. (3) can be used to compute the heat flow resistances from the wall temperature gradients and the temperature differences across the resistances. For regular operation, the wall temperatures gradients are then computed from the measured temperature differences and these resistances. Elimination of the heat transfer to the inside and the losses at both ends also enable calculation of h_{outside}, the heat transfer coefficient to the outside. It is computed (Eq. (2)) from the heat input and the fitted wall temperature distribution along the disconnected test section with insulated ends and blocked inside air passage. Generally, the gas temperature in the pipe can be calculated from the energy balance for a control volume extending from the pipe entry to the x-position in question,

$$\dot{m}c_p\left[T_{\text{gas}}(x) - T_{\text{gas}}(x_0)\right] = \int_0^x \left[\dot{q}'_{\text{heater}} - h_{\text{outside}}P(T_{\text{wall}} - T_{\text{ambient}})\right]\mathrm{d}x + \left[k_{\text{wall}}A_{\text{wall}}\frac{\mathrm{d}T_{\text{wall}}}{\mathrm{d}x}\right]_0^x. \quad (4)$$

Eq. (2) is evaluated at five axial locations where the resolution is limited by the number of thermocouples in the axial direction. Axially resolved Nusselt numbers are obtained from

$$\mathrm{Nu}_x = \frac{h_{\text{pipe}}D_{\text{hyd}}}{k} \quad (5)$$

in which property values are evaluated at the mean film temperature (arithmetic mean of wall and bulk gas temperature). A standard linearized error analysis is undertaken employing the root-mean-sum criterion; e.g., Tse and Morse (1989). The dominant error source in the axially resolved data stems from the heat redistribution caused by conduction along the manifold. This is because it is difficult to determine the second derivative of the wall temperature. Its local uncertainty is set to half the maximum value encountered along the complete axial length of the manifold. This error bound is chosen based on the robustness of the second temperature derivative to changes in the method used to fit the wall temperature.

Correlations are presented for both straight and curved manifold geometries at steady and pulsed flow. Within each data group, experimentally determined local Nu_x at all five axial locations and all airflow rates are curve fitted using the local Reynolds number and an expression in x/D_{hyd}. Axially averaged Nusselt numbers

$$\overline{\mathrm{Nu}} = \frac{1}{L}\int_0^L \mathrm{Nu}_x\,\mathrm{d}x \quad (6)$$

are also reported, where the integral is performed using the five local values for Nu_x. The error bounds for this integral are taken as the mean of the local error bounds except for the conduction term. Different treatment is appropriate, because errors in heat redistribution cancel when axially integrated. They are replaced by the uncertainty in the conduction losses at the ends. Uncertainty in any other quantity; e.g., the perimeter, tends to be the same over the whole axial extension and, hence, adds up. Therefore, the following expression is applied to estimate the uncertainty in the axially averaged Nusselt number,

$$\Delta\overline{\mathrm{Nu}} = \left(\left(\sum_{j=1}^{5}\frac{\partial \mathrm{Nu}_x}{\partial\alpha_{ij}}\Delta\alpha_{ij}\frac{L_j}{L}\right)^2 + \left(\frac{D_{\text{hyd}}}{K_{\text{gas}}}\frac{A_{\text{wall}}k_{\text{wall}}}{P(T_{\text{wall}} - T_{\text{gas}})}\frac{1}{L}\right)^2_{\max} \times\left[\left\{\Delta\left(\frac{\mathrm{d}T_{\text{wall}}}{\mathrm{d}x}\right)\right\}^2\right]_{x=0}^{x=L}\right)^{1/2}, \quad (7)$$

where j is the section index running from one to five, and α denotes any quantity entering Eq. (6) other than axial conduction.

4. Time-averaged results

Axially resolved experimental Nusselt numbers are computed from Eq. (2). In Fig. 3 these are compared to the literature values for steady flow in the straight duct geometry at a particular flow rate. The data are shown as multiples of the Nusselt number for fully developed pipe flow, as given by

$$\mathrm{Nu} = 0.023\,\mathrm{Re}^{0.8}\,\mathrm{Pr}^{0.4}. \quad (8)$$

The present results lie in the range of the previous findings for similar entrance configurations (note that the smooth bell-mouth entrance drawing air from an open atmosphere is expected to exhibit lower heat transfer rates). It is concluded that the apparatus and data evaluation procedure are adequate for investigating the other configurations where no literature data is available.

Data are correlated individually for the straight and the curved manifold to an expression in terms of Reynolds number and nondimensional distance from the entrance,

$$\mathrm{Nu}_x = a\,\mathrm{Re}_x^b\left[1 + c\exp\left(d\frac{x}{D_{\text{hyd}}}\right)\right]. \quad (9)$$

Property values are evaluated at the local arithmetic mean film temperature (typical gas and wall temperatures are 25°C and 60°C, respectively). The time-averaged axially resolved Reynolds number is evaluated from $\mathrm{Re}_x = \overline{U}(x)D_{\text{hyd}}/\nu(x) = 4\overline{\dot{m}}/\{\pi D_{\text{hyd}}\mu[T_{\text{film}}(x)]\}$, where $\overline{\dot{m}}$ is the measured time-mean mass flow rate. Because of thermal property variations, Re_x typically decreases by 2–3% along the axial length of the manifold runner. $\overline{\mathrm{Re}}$ is the axially (and temporally) averaged Reynolds number.

It would be desirable to add a frequency parameter to the correlation, to allow concurrent correlation of the steady and pulsating flow data into one expression. However, by utilizing a reciprocator with fixed stroke length to generate the pulsating flow, mean flow rate and pulsation frequency are closely related. As discussed in the Introduction section, flow velocities are approximately proportional to the frequency, and the mean to the peak velocity are at a fixed ratio. Only the mass flow rate is variable at a given engine speed, which is achieved by throttling the intake flow to lower densities. For both steady and pulsating flow, data are acquired at Reynolds numbers of approximately 3000, 8000, 18,000, 36,000. To attain these mean flow rates in the pulsating flow configuration, engine speeds are varied between 1000, 2500–2750, and 4500 rpm.

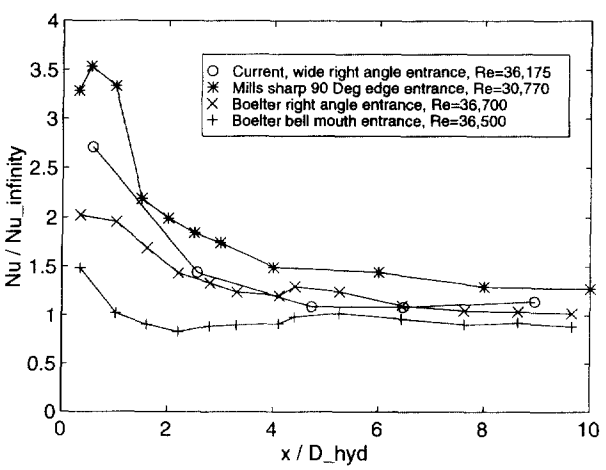

Fig. 3. Local Nusselt number divided by fully developed value: present data for steady flow in straight duct at particular Reynolds number in comparison to literature data.

and intake manifold absolute pressures are adjusted to 0.5 and 1.0 bar MAP. Two data pairs exhibit equal mean Reynolds numbers at different frequencies: $\overline{\mathrm{Re}} \approx 8000$ is attained both at 1000 rpm/1.0 bar MAP and 2500 rpm/0.5 bar MAP, and $\overline{\mathrm{Re}} \approx 18{,}000$ is measured for both 2750 rpm/1 bar MAP and 4500 rpm/0.5 bar MAP. Evaluation of candidate frequency parameters for the correlation is based on half of the engine rpm and the peak velocity as amplitude. The latter quantity is taken as $\hat{U} = 1.6 \times 4 \times \overline{U}$, where $\overline{U}$ is calculated from the above expression for $\overline{\mathrm{Re}}$. The factor of 4 accounts for the fact that flow is only during one quarter of the cycle, and the factor 1.6 relates the mean velocity over one stroke to the peak velocity. All frequency parameters reviewed in the Introduction section show only moderate changes over the given range of experimental conditions: $A = 16$–49, $\mathrm{Re}_\delta = 580$–2400, $\omega_1 = 10^{-4}$–10^{-3}, $\overline{\mathrm{Sr}} = 0.48$–$0.71$, and $\overline{\mathrm{Sr}}_{\bar{u}_1} = 7.5$–$11$. (The time-mean friction velocity is evaluated from the Blasius correlation using the time-averaged flow rate.) The data pairs with equal mean flow rate but different frequencies exhibit even smaller changes in frequency parameters, between 10 and 30%. It is concluded that no meaningful correlation with frequency is possible. Therefore, pulsating flow data are correlated separately from the steady flow data, thereby only employing the time-mean Reynolds number and axial distance as variables. The results show that heat transfer rates are close for the two paired groups at equal Reynolds number, giving justification to this approach (see Fig. 4). Note that the impact of wave dynamics is considered minor and is discussed in Section 5.

Table 3 lists the parameters a to d for each correlation Eq. (9). The deviation between correlation and data is well within the error-bars on the data and is not specified individually. An uncertainty analysis is performed as described above. The uncertainty is found to be less than 40% for high Reynolds numbers or near the entrance of the system (see Table 4). Because some of the loss terms are approximately constant, the relative uncertainty increases to 50–100% (160% in the worst case) for low heat transfer rates. These are encountered at downstream locations with low flow rates. Comparison between heat transfer rates of the different configurations reduces the uncertainties, because experimental procedures are kept the same. Because the findings compare well to literature values where available, it is assumed that the results are more precise than suggested by the above uncertainties.

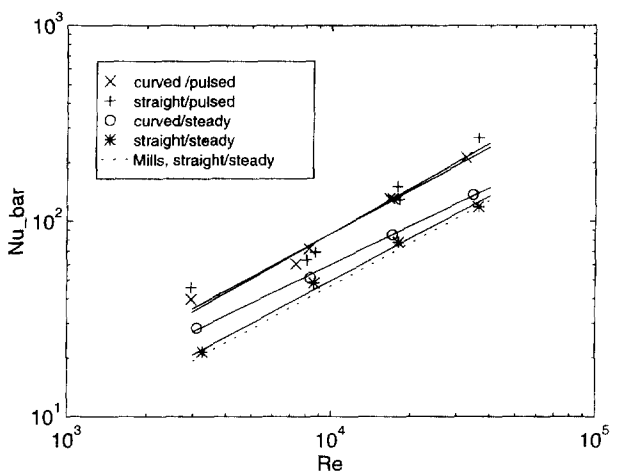

Fig. 4. Plot of measurements and correlations for local Nusselt number: steady and pulsating flow in curved and straight duct, comparison to literature value from Mills (1962).

Table 3
Coefficients of Nusselt number fit

Manifold/flow	a	b	c	d	e
Straight/steady	0.043	0.73	2.9	−0.68	0.062
Straight/pulsed	0.051	0.77	1.95	−0.49	0.072
Curved/steady	0.13	0.66	0.69	−1.05	0.14
Curved/pulsed	0.077	0.74	1.0	−0.42	0.10

The axially averaged Nusselt numbers (Eq. (6)) are correlated by the following

$$\overline{\mathrm{Nu}} = e\overline{\mathrm{Re}}^{b} \tag{10}$$

employing axially averaged values of the Reynolds number. The coefficient e is also given in Table 3. The uncertainty of the axially averaged data (and correlation) is typically less than 25% (with values up to 40% for the lowest Reynolds number, see Table 5). Fig. 4 plots the correlations along with the results of Mills (1962) for a sharp 90° entrance. Mill's data were for a straight manifold geometry and steady flow; the results for the corresponding current configuration agree well. Heat transfer in the curved pipe for steady flow is somewhat higher in comparison to the straight pipe, while it approximately doubles because of the engine intake flow pulsation for all Reynolds numbers with both manifolds. It is inferred that the entry and the flow pulsation generally have a stronger effect on heat transfer rates than the curvature.

The experiments do not show differences in heat transfer between motored and fired engine operation. Hot backflow from the cylinder into the intake, as it occurs especially during engine operation below atmospheric intake manifold pressures, does not reach the manifold test section, because it is sufficiently remote from the intake valve (10–45 cm). For an engine mounted in a car, heat transfer from the manifold runner to the charge gas also depends on the underhood thermal environment. Without quantitative knowledge of the heat transfer mechanism from the outside to the manifold pipe, heat transfer to the charge gas could be assessed by direct measurement of the manifold wall temperature. For a hypothetical wall temperature equal to a typical engine coolant temperature of 80°C and the engine running at a medium load and speed, charge temperature increase in the manifold runner computes

Table 4
Uncertainty associated with axially resolved Nusselt number correlation of Table 3; the larger uncertainties correspond to the lower Reynolds number limits

Manifold/flow	Re: 3000–9000		Re: 17,500–35,000	
	Entrance (%)	Exit (%)	Entrance (%)	Exit (%)
Straight/steady	<40	160–60	<40	<40
Straight/pulsed	<40	75–50	<40	<40
Curved/steady	60–40	90–50	<40	<40
Curved/pulsed	60–40	90–50	<40	<40

Table 5
Uncertainty associated with axially averaged Nusselt number correlation of Table 3

Manifold/flow	Re: 3000 (%)	Re: 8000–35,000 (%)
Straight/steady	50	<25
Straight/pulsed	<25	<25
Curved/steady	40	<25
Curved/pulsed	30	<25

to 20°C. This approximately corresponds to a 7% reduction in volumetric efficiency.

5. Time-resolved results

This section investigates the cause for the pulsating-flow heat transfer enhancement by means of time-resolved measurements of heat fluxes and other quantities. Fig. 5 plots the absolute of the phase-locked ensemble average of the velocity on the centerline for 2750 rpm/1 bar MAP operating condition. Absolute values below the calibration limit of 3.5 m/s are arbitrarily set to zero. Zero crank-angle corresponds to the bottom dead center position of the piston before the compression stroke. The induction flow is apparent from about 0° CA (crank angle) to 180° CA. The hump between 180° CA and 240° CA corresponds to a short backflow phase during the early part of the compression stroke caused by late intake valve closing. The smaller amplitude fluctuations are induced by pressure waves in the intake (most likely with alternating flow direction for each consecutive half wave).

Turbulence is produced close to the wall in a turbulent boundary layer, which then diffuses away from the wall. Turbulence measurements are shown in Fig. 5 for a location 2 mm from the wall. (For quasisteady conditions, y_+ would take values of 6, 60, and 300 at that location, for U equal to 1, 10, and 50 m/s, respectively. Peak turbulence intensities are typically 10% of the bulk velocity very close to the wall and drop to about 5% for $y_+ = 500$ and larger. Hence, this position is appropriate for discerning turbulence production for all encountered velocities.) The root-mean-square velocity fluctuation increases after intake valve opening as free-stream turbulence is convected into the test section. It further increases later during the induction flow. The most likely cause of this is the onset of turbulence production near the wall, which for pulsating flow conditions occurs late in the acceleration phase of the flow, Akhavan et al. (1991). With the deceleration of the flow, turbulence persists and decays slowly during the remainder of the cycle approximately following the solution of Malan and Johnston (1993), again see Fig. 5.

Figs. 6–8 show the experimental pressure, temperature, and heat flux traces (an adiabatic gas temperature is also plotted in Fig. 8 for comparison, based on the measured mean gas temperature and the experimental pressure data). During the closed portion of the cycle from 240° to 720° CA, pressure and temperature fluctuations are apparent with a frequency of approximately 200 Hz. As discussed in Section 1, these fluctuations induce significant heat flux fluctuations, because temperature changes also occur within the thermal boundary

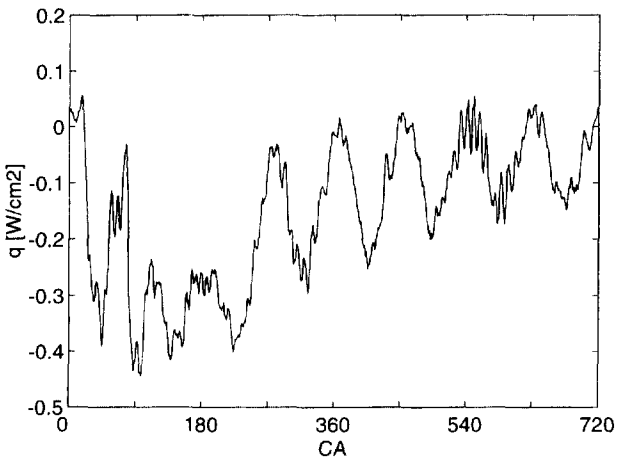

Fig. 6. Measured intake manifold pressure, 2750 rpm/1 bar MAP.

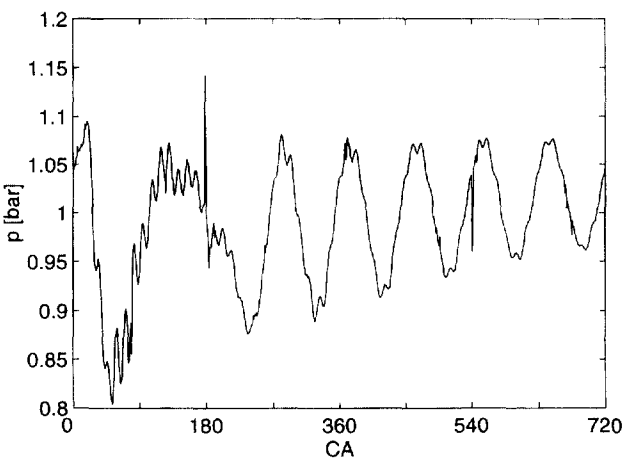

Fig. 7. Measured centerline gas temperature and calculated adiabatic gas temperature based on the measured mean temperature and the pressure fluctuation.

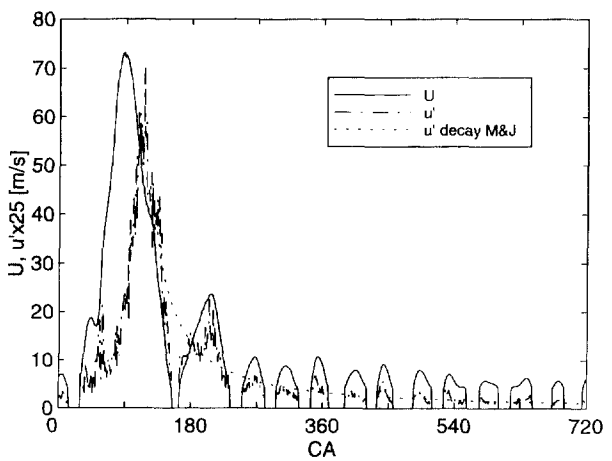

Fig. 5. Velocity measurement on centerline of straight pipe, turbulence intensity measurement 2 mm from the wall, 2750 rpm/1 bar MAP.

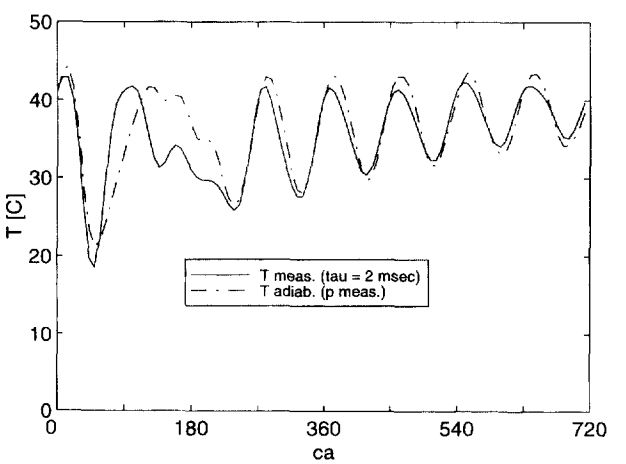

Fig. 8. Heat flux measurements 5 cm upstream of the exit of the straight manifold (positive sign into the wall), 2750 rpm/1 bar MAP.

layers. Fig. 9 compares a heat flux prediction based on the solution of Pfriem (1943) for periodic pressure fluctuations to the time-varying component of the measured signal $\tilde{q}''$ (signal minus time-mean of signal). It is apparent that many features of the measured signal are attributable to the pressure fluctuations.

The pressure-induced part of the signal can be subtracted from the total measured signal, and the difference should then constitute the convective and conductive heat transfer. Fig. 10 compares that difference to the turbulent steady flow correlation Eq. (8), and the numerical results of Malan and Johnston (1993). The latter are for heat transfer in a transiently growing shear free boundary layer. Their $Re_t = 380$ case is chosen for the comparison, to match the present estimated turbulent Reynolds number based on the measured turbulent intensity and a length-scale of one-tenth of the hydraulic diameter. The heat flux increase is somewhat delayed compared to the onset of forward flow. It eventually reaches values comparable to the steady situation. During flow deceleration, the heat fluxes again depart from quasisteady behavior in that they relax more slowly. There, they resemble the solution of Malan and Johnston (1993). The stagnant phase obviously contributes strongly to the total heat transfer, explaining why heat transfer is elevated for pulsating flow above the steady-state values. Integrating the ratio of the transient heat flux over the difference of the wall to the transient gas temperature yields the time-averaged heat transfer coefficient. This mean heat transfer coefficient is $61 \pm 23\,W/m^2$-K, which compares quite well to the corresponding time-averaged value obtained in the experiment described previously, $89 \pm 25\,W/m^2$-K.

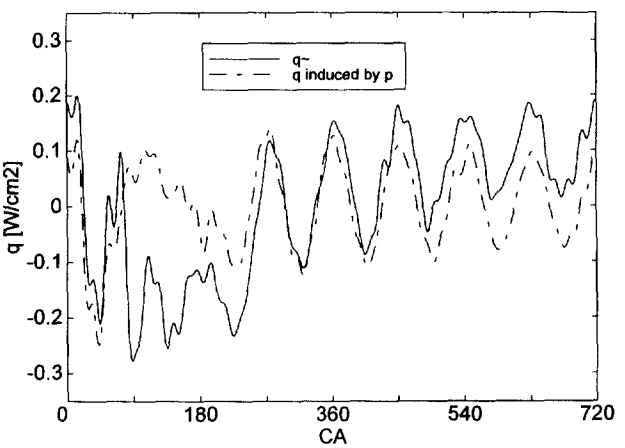

Fig. 9. Comparison of heat flux prediction using the solution of Pfriem (1943) for periodic pressure fluctuations to the time-varying component of the measured signal, 2750 rpm/1 bar MAP.

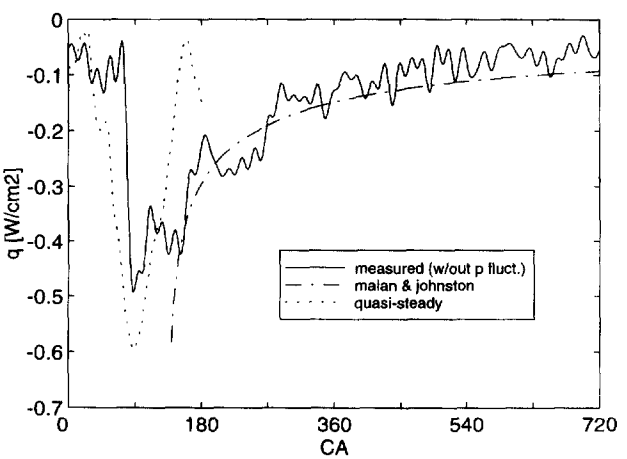

Fig. 10. Measured heat flux after subtraction of pressure wave-induced component in comparison to steady-state correlation (~0°–180°CA), and the solution of Malan and Johnston's (1993) (~180°–720°CA), 2750 rpm/1 bar MAP.

6. Summary and conclusions

Experiments were conducted to determine heat transfer rates in the intake pipe (manifold runner) of internal combustion engines. It is expected that the results also apply to the corresponding components of compressors and other devices where pulsating flows with stagnant phases occur. Two ducts, one straight and one highly curved, were employed, which together bracket most realistic geometries. Heat transfer results for the straight pipe and steady flow compared well to previous findings. Heat transfer in the highly curved duct was comparable to that in the straight one, suggesting that entrance effects dominated over secondary flow phenomena. Heat transfer under real (pulsating) flow conditions was found to double as compared to the steady flow case, which was further investigated by time-resolved measurements. Time-averaged, axially resolved and axially averaged Nusselt numbers were correlated with Reynolds number. The pulsating flow data were not correlated with an additional frequency variable, because engine rpm and mean flow rate were approximately coupled. Similarly, the amplitude ratio or waveform of the pulsating flow was given through the employed engine and not altered during the experiments.

Time-resolved measurements showed that wave dynamics induced significant heat fluxes. These were closely comparable to predictions employing the solution of Pfriem (1943) for heat fluxes induced by periodic pressure variations. As their net contribution canceled over one cycle, they were subtracted from the original heat flux signal. The time-resolved measurements then showed that heat transfer rates were on the order of quasisteady values during the main flow phase. The stagnant phase (three-quarters of the cycle) contributed just as much to the total heat transfer as the main induction flow. This was attributed to the slow decay of the turbulence generated during the induction flow. Heat transfer rates in the stagnant phase were similar to the prediction of Malan and Johnston (1993) for a shear-free turbulent boundary layer. For applications that require temporal resolution, it is clearly inappropriate to assume quasisteady heat transfer behavior.

Acknowledgements

This work has been sponsored by the Ford Powertrain Research Laboratory in Dearborn, MI, USA. Special thanks to Dr. Stephen Russ and William Stockhausen, both at Ford, for their input and ongoing review of our work. Also thanks to Neeta Verma and Charles Tam who helped build the experimental apparatus while working as undergraduate research assistants at the M.I.T. Sloan Automotive Laboratory. We appreciate the help that Stefan Grönniger gave us while he was here as a visiting student from the RWTH in Aachen, Germany. This work has benefited from the input from several M.I.T. faculty: Professors R.D. Kamm, J.B. Lienhard, J. Smith, and W.K. Cheng. Finally, we acknowledge Adam Baker from Engineering Department of Cambridge University in the UK,

who read the draft version of this paper and gave us access to his currently unpublished literature review on heat transfer in unsteady duct flow.

References

Akhavan, R., Kamm, R.D., Shapiro, A.H., 1991. An investigation of transition to turbulence in bounded oscillatory stokes flows, Part 1. Experiments. J. Fluid Mech. 225, 395–422.

Arpaci, V.S., Dec, J.E., Keller, J.O., 1993. Heat transfer in pulse combustor tailpipes. Combust. Sci. Tech. 94, 131–146.

Boelter, L.M.K., Young, G., Iversen, H.W., 1948. An investigation of aircraft heaters XXVII – Distribution of heat transfer rates in the entrance section of a circular tube. NACA, TN 1451.

Borman, G., Nishiwaki, K., 1987. Internal combustion engine heat transfer. Prog. Energy Combust. Sci. 13, 1–46.

Condie, K.G., McEligot, D.M., 1995. Convective heat transfer for pulsating flow in the takedown pipe of a V-6 Engine. SAE paper 950618.

Liao, N.-S., Wang, C.-C., 1988. On the convective heat transfer in pulsating turbulent pipe flow. In: Shah, P.K. et al. (Ed.), Proc. 1st World Conf. on Experimental Heat Transfer, Fluid Mechanics, and Thermodynamics, Dubrovnik, 1988, pp. 536–542.

Malan, P., Johnston, J.P., 1993. Heat transfer in shear-free turbulent boundary layers. Thermosciences Division, Department of Mechanical Engineering, Stanford University, Stanford, CA, Report MD-64.

Mills, A.F., 1962. Experimental investigation of turbulent heat transfer in the entrance region of a circular conduit. J. Mech. Eng. Sci. 4, 63–77.

Pfriem, H., 1943. Periodic heat transfer at small pressure fluctuations. NACA 4, 63–77.

Pratt, N.H., 1947. The heat transfer in a reaction tank cooled by means of a coil. Trans. Inst. Chem. Eng. 25, 163–180.

Schmidt, E.F., 1967. Wärmeübergang und Druckverlust in Rohrschlangen. Chem. Ing. Tech. 39, 781–789.

Tse, F.S., Morse, I.E., 1989. Measurement and Instrumentation in Engineering. Marcel Dekker, New York.